# Novel Data-Driven Spatial-Spectral Correlated Scheme for Dimensionality Reduction of Hyperspectral Images

Yanming Zhang, *Student Member, IEEE*, Ping Yuan, Lijun Jiang, *Fellow, IEEE*, and Hong Tat Ewe, *Senior Member, IEEE*

***Abstract*—Hyperspectral imaging technology has been popularly applied in remote sensing because it collects echoed signals from across the electromagnetic (EM) spectrum and thereby contributes fruitfully spatial-spectral information. However, the processing or storage of high-data-volume hyperspectral images (HSIs), also viewed as snapshots varying with the EM spectrum, burdens the hardware resources, especially for the high spectral resolution and spatial resolution cases. To address this challenge, a novel unsupervised dimensionality reduction method based on the dynamic mode decomposition (DMD) algorithm is proposed to analyze hyperspectral data. This method decomposes the spatial-spectral HSIs in terms of spatial dynamic modes and corresponding spectral patterns. Then, these spatial-spectral patterns are combined to reconstruct the raw HSIs via a low-rank model. Furthermore, we extend the proposed DMD method to hyperspectral data in the tensor form and title it CubeDMD to actualize the compression of HSIs in horizontal, vertical, and spectral dimensions. Our proposed data-driven scheme is benchmarked by the real hyperspectral data measured at the Salinas scenes and Pavia University. It is demonstrated that the HSIs can be reconstructed accurately and effectively by the proposed low-rank model. The mean peak signal-to-noise ratio between the reconstructed and original HSIs can reach 31.47 dB, and the corresponding mean spectral angle mapper is only 0.1037. Our work provides a useful tool for the analysis of HSIs with a low-rank representation.**

***Index Terms*—Cube dynamic mode decomposition (CubeDMD), hyperspectral images (HSIs), reconstruction, three-order tensor, unsupervised dimensionality reduction.**

## I. Introduction

HYPERSPECTRAL images (HSIs), a set of photographs of the same observation scene measured from across the electromagnetic (EM) spectrum, have been extensively employed in classifying objects [1]–[4], detecting targets [5]–[7], and extracting terrain features [8]–[11]. Herein, different objects uniquely reflect, absorb, and emit EM radiation according to their molecular composition, roughness, and texture [2]. Based on this, hyperspectral imaging technology collects the objects' radiation within a wide range of EM frequencies. It allows HSIs to provide not only spatial but also spectral information of the observed objects. However, advanced developments of HSIs, such as a high-dimensional spatial domain with higher resolution and larger spectral channels, bring challenges to their storage and processing [6]. For example, storage of 16 bits-per-pixel-per-band HSIs with 500 spectral channels and $600 \times 400$ pixels in spatial dimension consumes 320 megabytes (MB) computer memory. Moreover, in the time-varying hyperspectral observation, the amount of collected data increases linearly with time, which will induce the curse of dimensionality. To tackle this issue, various dimensionality reduction algorithms have been developed for the compression of HSIs. To sum up, we have categorized seminal contributions into three types as follows.

1) *Unsupervised scheme:* Unsupervised dimensionality reduction methods are generally used for the nonlabeled hyperspectral data that is directly obtained from the measurement. Unsupervised methods achieve the compression of HISs by setting some criteria to find the representation in low-dimensional space. A chain of unsupervised dimensionality reduction approaches has been developed, such as principal component analysis (PCA) [9], singular value decomposition (SVD) [12], minimum noise fraction (MNF) transform [10], and independent component analysis (ICA) [11]. Afterward, several new criteria are developed for unsupervised dimensionality reduction in manifold learning-based methods, such as locality-preserving projections [13], neighborhood embedding feature selection [14], and local neighborhood structure-preserving embedding [15]. The superpixel-wise PCA method optimizes the dimensionality reduction effect of traditional PCA by taking the diversity in different homogeneous regions into account [16]. Recently, WavCycleGAN is developed using the wavelet directional method to realize the reconstruction of HSIs with noise removal and without sacrificing HSIs' high-frequency components [17]. The nonlinear autoencoder method is proposed

Manuscript received January 19, 2022; revised March 25, 2022; accepted May 6, 2022. Date of publication May 10, 2022; date of current version May 23, 2022. This work was supported in part by the Research Grants Council of Hong Kong under Grant GRF 17209918, Grant GRF 17207114, and Grant GRF 17210815, in part by the Asian Office of Aerospace Research and Development under Grant FA2386-17-1-0010, in part by the National Natural Science Foundation of China under Grant 61271158, in part by HKU Seed Fund under Grant 104005008 and Grant 201711159228, and in part by Hong Kong University under Grant AoE/P-04/08. *(Corresponding author: Lijun Jiang.)*

Yanming Zhang, Ping Yuan, and Lijun Jiang are with the Department of Electrical and Electronic Engineering, University of Hong Kong, Hong Kong (e-mail: ymzhang@eee.hku.hk; yuanp019@connect.hku.hk; ljiang@eee.hku.hk).

Hong Tat Ewe is with the Department of Electrical and Electronic Engineering, Universiti Tunku Abdul Rahman (UTAR), Kuala Lumpur 43000, Malaysia (e-mail: eweht@utar.edu.my).

Digital Object Identifier 10.1109/JSTARS.2022.3173999

This work is licensed under a Creative Commons Attribution 4.0 License. For more information, see https://creativecommons.org/licenses/by/4.0/

for dealing with HSIs' nonlinear mixing terms [18]. Multiple kernel learning and self-organizing maps are integrated to represent multiscale fuse features of large HSIs [19].

2) *Supervised scheme:* This scheme relies on the labeled hyperspectral data to infer class separability. A variety of supervised dimensionality reduction approaches have been proposed. Li *et al.* [20] combined the multinomial logistic regression (MLR) and Markov random fields to, respectively, deal with the spectral and spatial information for the segmentation of HSIs. Cao *et al.* [21] explored the local and global sparse representation to improve the dimensionality reduction performance of HSIs in both spectral and spatial domains. With the recent popularity of deep learning, supervised dimensionality reduction methods based on convolutional neural networks (CNNs) have become a new trend. Hereinto, Zeegers *et al.* [7] propose an end-to-end architecture for data reduction with more image compression and higher accuracies. Bayesian CNNs are trained for hyperspectral image classification with high performance via active learning in [1]. Maximum overlap pooling CNNs [5] is proposed to improve the details of HSIs and obtain a high classification accuracy via avoiding the fuzziness of average pooling.
3) *Semisupervised scheme:* Semisupervised schemes are explored to solve the bottleneck of the limited labeled data. In practice, labeling a large number of samples may require considerable human resources or expertise. Unlabeled data, however, are more conveniently available in large quantities at an economical cost. Consequently, semisupervised schemes are comprehensively investigated via using both unlabeled and limited labeled data in the classification [22], [23]. For example, Li *et al.* [24] integrated MLR and active learning approach. He *et al.* [25] proposed an optimal graph approach for the band selection of HSIs. These methods combine the advantages of the supervised scheme and unsupervised methods. They can achieve optimal results given a limited set of specific HSI data.

The aforementioned methods are mainly applied to the matrix representation of the HSIs, which needs the reshaping process of hyperspectral data cube in prior. More recently, it has been demonstrated that compared with processing HSIs based on matrix representation, dimensionality reduction of hyperspectral data in the tensor form can achieve a higher compression ratio [26]. Hence, it is necessary to realize dimensionality reduction directly based on high-dimensional tensor representation. To this end, significant work has been performed from different perspectives. In Category 1), the multilinear PCA method is investigated for tensor HSIs with object feature extraction [6], [26], [27]. Afterwards, An *et al.* [28] determine the optimal low rank of HSIs via tensor-based multiscale decomposition. In Category 2), various studies have been carried out by directly dealing with hyperspectral tensor form via tensor CNNs [29], [30], tensor neighborhood graph [31], [32], and modified tensor patch [33]. In Category 3), the labeled and unlabeled data are combined within the tensor form and then processed for compression and classification [34], [35]. It is worth noting that a more detailed literature review can be found in Section III of [2], and here we mainly review the latest published work as a supplement.

While the studies mentioned earlier have achieved significant developments, it is still an open and challenging issue to represent the HSIs with dimensionality reduction. The desirable low-rank reconstruction requires a small memory space, the expression as realistic as possible, and convenient calculation in the form of a matrix or tensor. Notably, the main challenge of the unsupervised approach is that it lacks the ability to integrate spatial and spectral information in the dimensionality reduction of HSIs [21].

In this article, we investigate the dynamic mode decomposition (DMD) approach to reduce the dimension of HSIs with the unsupervised scheme. Through the DMD method, the spatial-spectral hyperspectral data is decomposed into the spatial modes and corresponding spectral patterns. Each spatial mode varies exponentially with the index of EM bands, which is solely determined by its corresponding spectral pattern. Then, these decomposed patterns reconstruct the original hyperspectral data via the low-dimensional linear combination. Recently, the traditional DMD method is used in the analysis of the HSIs represented by the matrix [36]. We further explore the cube dynamic mode decomposition (CubeDMD) method to reduce the dimensionality of HSIs in the form of tensors. Some measured HSIs are used to validate the proposed method. It is worth noting that, as an unsupervised scheme, the proposed method integrates the spatial and spectral correlation information for further improvement of the performance on the reconstruction of HSIs. Also, the dimensionality reduction is obtained not only in the spectral domain but also in the spatial domain. Our contributions lie in several aspects as follows.

1) We establish the DMD-based approach for dimensionality reduction of HSIs. Herein, the HSIs are represented by a low-dimensional spatial-spectral correlated state-space, where the variation of spatial distribution is only determined by the eigenvalues in the spectrum. Unlike the SVD that uses the same number of spectral dimension's elements as the original data to represent HSIs, DMD only uses fewer eigenvalues and a fixed exponential form to reconstruct the spectral distribution.
2) Our proposed data-driven method is with an unsupervised scheme. Thus, comparing the supervised scheme and semisupervised scheme, cumbersome labeling workload and training process are avoided.
3) According to the nature of the cube shape of hyperspectral data, we further develop a modified DMD method based on the tensor form, namely CubeDMD. Compared with DMD, CubeDMD can further compress the horizontal and vertical dimension in the spatial domain, which ensures that HSIs can be reconstructed from a data form with less than the original spatial dimension, to compress the horizontal and vertical dimension in the spatial domain. The quantitative analysis of the reconstruction results demonstrates its effectiveness and accuracy.

Hence, the proposed state-of-the-art data-driven scheme could be an effective tool for dimensionality reduction of HSIs.

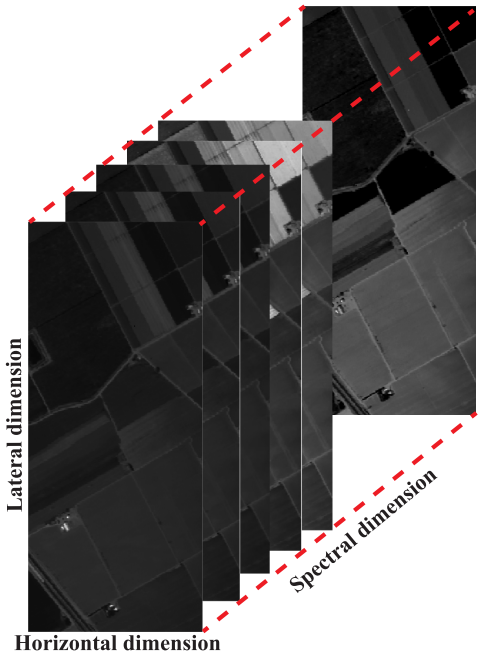


Fig. 1. Schematic of a hyperspectral data cube.

The remainder of this article is formed as follows. Section II introduces the adopted notations and the background. In Section III, we propose DMD and CubeDMD to reduce the dimensionality of HSIs in matrix and tensor form, respectively. Results based on experimental HSIs are benchmarked to verify the proposed methods in Section IV. Finally, Section V concludes this article.

## II. Background

### A. Notations

A tensor often refers to the multidimensional array, and its dimensions' number is expressed as the order of a tensor. In this article, we adopt the lowercase Latin letters, e.g., $a, b, c, \ldots$, to denote the scalars (zero-order tensors), the lowercase bold-face Latin letters, e.g., $\mathbf{a}, \mathbf{b}, \mathbf{c}, \ldots$, to denote the vectors (first-order tensors), the uppercase bold-face Latin letters, e.g., $\mathbf{A}, \mathbf{B}, \mathbf{C}, \ldots$, to denote the matrices (second-order tensors), and the bold calligraphy Latin letters, e.g., $\mathcal{A}, \mathcal{B}, \mathcal{C}, \ldots$, to the higher-order tensor. Without loss of generality, $N$-order tensor can be expressed as $\mathcal{T} \in \mathbb{R}^{I_1 \times I_2 \times \cdots \times I_k \times \cdots \times I_N}$. Herein, $I_k$ is often larger than 1 and denotes the dimension of the $k$th mode. $\mathbb{R}$ denotes the real analytic space.

### B. Hyperspectral Data Cube

As shown in Fig. 1, the spatial-spectral HSIs is often regarded as a three-dimensional data cube. To be specific, we can use a three-order tensor $\mathcal{T}(i_1, i_2, i_3)$ (or the subscript form: $\mathcal{T}_{i_1,i_2,i_3}$ to represent HSIs). Hereinto, $i_1$ and $i_2$ refer to the horizontal ($x$) and lateral dimension ($y$) in the spatial domain, respectively. $i_3$ solely denotes the spectral dimension, which represents the observation with a specific EM frequency ($\lambda$). To be specific, we assume that $d(x_i, y_j, \lambda_l), i = 1, \ldots, O, j = 1, \ldots, P$, and $l = 1, 2, \ldots,$ L denote a pixel measured at a specific EM spectrum. If the vector $\mathbf{r} = (x, y)$ is defined to represent the spatial domain, one can obtain a set of snapshots varying with the EM spectrum, which is expressed as follows.

$$\mathbf{D} = \begin{bmatrix} d(\mathbf{r}_1, \lambda_1) & \cdots & d(\mathbf{r}_1, \lambda_l) & \cdots & d(\mathbf{r}_1, \lambda_L) \\ \vdots & \cdots & \vdots & \cdots & \vdots \\ d(\mathbf{r}_M, \lambda_1) & \cdots & d(\mathbf{r}_M, \lambda_l) & \cdots & d(\mathbf{r}_M, \lambda_L) \end{bmatrix} \in \mathbb{R}^{M \times L} \tag{1}$$

Here $M = O \times P$ denotes the number of pixels in each image, and $l$th column of $\mathbf{D}$ means the observation sequence $\mathbf{d}_l$, also named as the $l$th snapshot. Then, the raw hyperspectral data can be expressed by a matrix as $\mathbf{D} = [\mathbf{d}_1, \mathbf{d}_2, \ldots, \mathbf{d}_l, \ldots, \mathbf{d}_L]$.

### C. Singular Value Decomposition

SVD is a factorization method of any real-valued and complex-valued matrix, which has been widely studied and applied for the dimensionality reduction of HSIs [12], [37]–[39]. Specifically, $\mathbf{D}$ in (1) is used as an example. Through SVD, we have

$$\mathbf{D} = \mathbf{U}\mathbf{S}\mathbf{V}^H \tag{2}$$

where the superscript $H$ denotes the Hermitian transpose. $\mathbf{S}$ is the diagonal matrix of size $r \times r$. Its diagonal elements are denoted as $\sigma_i$, which refer to singular values of SVD. $\sigma_i$ is a non-negative real number and usually sorted in decreasing order as follows:

$$\sigma_1 \geq \sigma_2 \geq \cdots \geq \sigma_r \geq 0. \tag{3}$$

$\mathbf{U}$ and $\mathbf{V}$ denote an $M \times r$ and $L \times r$ semiunitary matrix, respectively. Namely, one can obtain $\mathbf{U}^H\mathbf{U} = \mathbf{V}^H\mathbf{V} = \mathbf{I}_{r \times r}$. The columns of $\mathbf{U}$ and $\mathbf{V}$ refer to the left and right singular vectors, respectively, which also correspond to the singular values $\sigma_i$. It is worth noting that there are two implementations of SVD, namely compact SVD and truncated SVD. In the compact SVD scheme, $r$ is directly set to $\min\{M, L\}$. When the rank of $\mathbf{D}$ is less than $\min\{M, L\}$, the truncated SVD is adopted via setting a threshold $\varepsilon_{\text{SVD}}$ to select the first $r^*$-order singular values. The formula for selection is as follows:

$$\sqrt{\frac{\sigma_{r^*+1}^2 + \cdots + \sigma_r^2}{\sigma_1^2 + \cdots + \sigma_r^2}} \leq \varepsilon_{\text{SVD}}. \tag{4}$$

By such truncation, an approximation of $\mathbf{D}$ can be achieved by a low-rank representation. Besides, a proper truncation selection in SVD is a beneficial way of removing the noise of HSIs.

### D. Higher Order Singular Value Decomposition

When dealing with multidimensional data, SVD needs to be extended to handle tensors of order greater than two. Several such extensions have been investigated to solve this nontrivial task, such as canonical decomposition [40], tensor singular value decomposition (t-SVD) [6], and higher order singular value decomposition (HOSVD) [41]–[43]. Hereinto, the higher order singular value decomposition (HOSVD) first proposed by Tucker [41] has been proven to have high

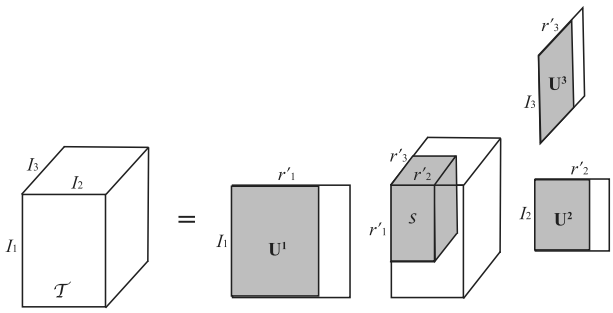


Fig. 2. Illustration of the HOSVD of a hyperspectral data cube (three-order tensor).

robustness [42], [43] and is widely used in multidimensional signal processing [44]–[46]. In specific, we take $\mathcal{T}_{i_1,i_2,i_3}$ shown in Fig. 1 as an example. Through the HOSVD, one can obtain

$$\mathcal{T}_{i_1,i_2,i_3} = \sum_{n_1=1}^{r_1'} \sum_{n_2=1}^{r_2'} \sum_{n_3=1}^{r_3'} \mathcal{S}_{n_1 n_2 n_3} \mathbf{U}^1_{i_1 n_1} \mathbf{U}^2_{i_2 n_2} \mathbf{U}^3_{i_3 n_3} \quad (5)$$

where $r_1', r_2'$, and $r_3'$ refer to the ranks of the fibers of the HSIs' tensor along the horizontal, lateral, spectral dimensions. The vector $\mathbf{r} = (r_1', r_2', r_3')$ is defined as the multilinear rank of the tensor $\mathcal{T}$. $\mathcal{S}_{n_1 n_2 n_3}$ represents the components of the three-order tensor $\mathcal{S}$ that means the core tensor of size $r_1' \times r_2' \times r_3'$. The matrices $\mathbf{U}^1, \mathbf{U}^2, \mathbf{U}^3$, of sizes $I_1 \times r_1', I_2 \times r_2', I_3 \times r_3'$, respectively, whose elements are $\mathbf{U}^1_{i_1 n_1}$, $\mathbf{U}^2_{i_2 n_2}$, and $\mathbf{U}^3_{i_3 n_3}$, respectively, refer to the mode matrices along the horizontal, lateral, and spectral dimensions of the HSIs. Visualization of the HOSVD for the $\mathcal{T}$ is presented in Fig. 2 for better understanding.

## III. Methods

In this section, we will present the proposed data-driven scheme for the compression of HSIs. The DMD method is first detailed for the matrix form HSIs. Then, the CubeDMD is given for the tensor form HSIs based on the fact that their data set is a cube.

### A. Dynamic Mode Decomposition

The DMD method was first proposed in the field of hydrodynamics [47] and then widely applied in many fields, such as EM vortex beams [48]–[50], power system [51], sea clutter [52], ship wake detection [53], and chaos system [54]. Traditionally, DMD decomposes the spatial-temporal signal by the low-dimensional exponential modes with the corresponding oscillation frequency and decay/growth rate [47]. Interestingly, there is an analogy between the time-varying snapshots and HSIs, which can be viewed as "EM frequency-varying" snapshots. So, when low-rank representation can be obtained by providing the time series of data through DMD, we should be able to obtain dimensionality reduction of HSIs. Here, we take matrix $\mathbf{D}$ in (1) as an example to illustrate the process of the DMD method. Specifically, it is assumed that the mapping relationship between the two adjacent observation sequences in $\mathbf{D}$ is linear, which can be expressed as

$$\mathbf{d}_{l+1} \simeq \mathbf{Q}\mathbf{d}_l \quad \text{for } l = 1, \ldots, L-1. \quad (6)$$

Here, $\mathbf{Q}$ denotes the mapping matrix with size of $M \times M$, whose eigenvalues and eigenvectors grasp the main dynamic characteristics of HSIs. Based on this linear assumption, the solution on the state-space of the HSIs could be expressed as [55]

$$\mathbf{d}_l \simeq \sum_{n=1}^{N} a_n \mathbf{q}_n e^{(\delta_n + \mathrm{i}\omega_n)(l-1)\Delta\lambda} \quad (7)$$

where $\mathbf{d}$ refers to a spectrum-dependent vector of size $M$. $\mathbf{q}_n$ refers to the $n$th spatial mode, $a_n$ denotes the corresponding mode amplitude, and $\delta_n$ and $\omega_n$ refer to the associated damping rate and frequency, respectively. $\Delta\lambda$ means the interval of the HSIs spectral dimension. Since the index of the EM band is assumed to represent the spectral dimension here, $\Delta\lambda$ is equal to 1. Notably, through this spatial-spectral correlated representation, HSIs can be jointly expressed by the spectral space in terms of an exponential pattern and the associated spatial modes. The goal of the DMD method is to obtain this expression merely from the hyperspectral data. In the following, we will introduce how to compute the coefficients in (7) via the DMD approach.

For convenience of notation, we define $\mathbf{D}_{l_1}^{l_2}$, in which $l_1 < l_2$, to represent the snapshot matrix, and its columns are the observation sequences with indices between $l_1$ and $l_2$, such that $\mathbf{D}_{l_1}^{l_2} = [\mathbf{d}_{l_1}, \mathbf{d}_{l_1+1}, \ldots, \mathbf{d}_{l_2}]$. We split the data matrix $\mathbf{D}$ into two snapshot matrices, namely $\mathbf{D}_1^{L-1}$ and $\mathbf{D}_2^{L}$. Then, the relation in the (6) can be rewritten in terms of these two snapshot matrices as follows:

$$\mathbf{D}_2^L \simeq \mathbf{Q}\mathbf{D}_1^{L-1}. \quad (8)$$

Based on this assumption, the DMD method can express the system state with a low-rank model in three steps.

*1) Dimension Reduction:* First, this step decomposes the first sequence matrix $\mathbf{D}_1^L$ with the SVD approach in (2), which is given as

$$\mathbf{D}_1^L \simeq \mathbf{U}\mathbf{S}\mathbf{V}^H \quad (9)$$

where $\mathbf{U}^H\mathbf{U} = \mathbf{V}^H\mathbf{V} = \mathbf{I}_{\tilde{N}\times\tilde{N}}$; the matrix $\mathbf{U}$ with size of $M \times \tilde{N}$ and $\mathbf{V}$ with size of $L \times \tilde{N}$ refers to the spatial and spectral SVD modes, respectively; and $\mathbf{I}_{\tilde{N}\times\tilde{N}}$ refers to a unit matrix of order $\tilde{N}$. Hereinto, $\tilde{N}$ denotes the number of truncated SVD modes, which is determined according to (4). Notably, through the SVD approach, the original states in the HSIs are represented in a low-dimensional system. From now on, the letters with tildes, $\tilde{\cdot}$, are adopted to denote the state in this dimensionality reduction system. The reduced snapshot matrix in this low-dimensional system is defined as $\tilde{\mathbf{D}}_1^L = \mathbf{S}\mathbf{V}^H$. Also, the columns of $\tilde{\mathbf{D}}_1^L$ are named as the the reduced snapshots, which can be expressed as follows:

$$\tilde{\mathbf{D}}_1^L = \left[\tilde{\mathbf{d}}_1, \tilde{\mathbf{d}}_2, \ldots, \tilde{\mathbf{d}}_L\right]. \quad (10)$$

Then, the matrix $\mathbf{U}$ can be used to connect the original dimensional system and the low-dimensional system, and one can obtain $\mathbf{D}_1^L = \mathbf{U}\tilde{\mathbf{D}}_1^L$ or $\tilde{\mathbf{D}}_1^L = \mathbf{U}^H\mathbf{D}_1^L$. The reduced snapshots exhibit a much smaller dimension than the original snapshots if $\tilde{N} \ll L$, which is the usual case for HSIs with multiple spectral channels. That is to say, this redundancy in HSIs can admit a significant dimension reduction. Then, we calculate the parameters of (7), including the damping rates, frequencies,

and mode amplitude, all in this reduced-dimension space. In particular, $\mathbf{D}_1^N = \mathbf{U}\tilde{\mathbf{D}}_1^N$ implies that the snapshots and reduced snapshots are related as

$$\mathbf{d}_l \simeq \mathbf{U}\tilde{\mathbf{d}}_l \tag{11}$$

or

$$\tilde{\mathbf{d}}_l \simeq \mathbf{U}^H \mathbf{d}_l. \tag{12}$$

Premultiplying (7) by $\mathbf{U}^H$, one can obtain

$$\tilde{\mathbf{d}}_l \simeq \sum_{n=1}^{\tilde{N}} a_n \tilde{\mathbf{q}}_n e^{(\delta_n + \mathrm{i}\omega_n)(l-1)\Delta\lambda} \tag{13}$$

where the reduced spatial mode, $\tilde{\mathbf{q}}_n = \mathbf{U}^H \mathbf{q}_n$, refers to the DMD mode. It is worth noting that once the expansion of (13) is computed, which is explained in the next step in detail, the original expansion of (7) can be obtained via premultiplying (13) by $\mathbf{U}$, in which $\mathbf{q}_n = \mathbf{U}\tilde{\mathbf{q}}_n$.

*2) Computation of Damping Rates $\delta_n$ and Frequencies $\omega_n$:* This step calculates the aforementioned parameters via the newly constructed reduced mapping matrix, $\tilde{\mathbf{Q}}$, which is defined as

$$\tilde{\mathbf{Q}} = \mathbf{U}^H \mathbf{Q} \mathbf{U}. \tag{14}$$

Then, the relationship in (6) and (8) can be reexpressed in the low-dimensional space as

$$\tilde{\mathbf{d}}_{l+1} \simeq \tilde{\mathbf{Q}}\tilde{\mathbf{d}}_l \tag{15}$$

and

$$\tilde{\mathbf{D}}_2^L \simeq \tilde{\mathbf{Q}}\tilde{\mathbf{D}}_1^{L-1}. \tag{16}$$

To construct $\tilde{\mathbf{Q}}$, SVD is first implemented for the $\tilde{\mathbf{D}}_1^{L-1}$, such that

$$\tilde{\mathbf{D}}_1^{L-1} = \tilde{\mathbf{U}}\tilde{\mathbf{S}}\tilde{\mathbf{V}}^H. \tag{17}$$

Substituting (17) into (16), one can obtain

$$\tilde{\mathbf{D}}_2^L = \tilde{\mathbf{Q}}\tilde{\mathbf{U}}\tilde{\mathbf{S}}\tilde{\mathbf{V}}^H. \tag{18}$$

Then, postmultiplying (18) by $\tilde{\mathbf{V}}\tilde{\mathbf{S}}^{-1}\tilde{\mathbf{U}}^H$, we have

$$\tilde{\mathbf{Q}} = \tilde{\mathbf{D}}_2^L \tilde{\mathbf{U}}\tilde{\mathbf{S}}\tilde{\mathbf{V}}^H. \tag{19}$$

It is clear that the reduced mapping matrix $\tilde{\mathbf{Q}}$ has been obtained based on the reduced snapshots. Then, the general solution of (15) expressed as (13) can be obtained via the eigen decomposition of $\tilde{\mathbf{Q}}$, in which $\mathbf{p}_n$ and $\xi_n$ are used to denoted the eigenvectors and associated eigenvalues of $\tilde{\mathbf{Q}}$, respectively. We have

$$\tilde{\mathbf{d}}_l = \sum_{n=1}^{\tilde{N}} a_n \mathbf{p}_n \xi_n^{l-1} \tag{20}$$

where the eigenvectors of $\mathbf{p}_n$ refer to the $\tilde{\mathbf{q}}_\mathbf{n}$, namely $\mathbf{p}_n = \tilde{\mathbf{q}}_\mathbf{n}$, and the associated eigenvalues $\tilde{\xi}_n$ imply the damping rates and the frequency, such that $\delta_n + \mathrm{i}\omega_n = 1/(\Delta\lambda)\,\log \xi_n$. The distribution of the damping rates and the frequency is also denoted as the DMD spectrum. Notably, all the derivations of parameters in the targeted expression are implemented in a low-dimensional space. It can significantly reduce memory consumption during processing high-data-volume HSIs.

*3) Computation of the Mode Amplitudes:* This last step is to calculate the mode amplitude $a_n$. Hereinto, the left-hand side of (20), $\tilde{\mathbf{d}}_l$, is the known reduced snapshots with the size of $\tilde{N}$, and $\tilde{N}$ eigenvectors $\mathbf{p}_n$ and eigenvalues $\tilde{\xi}_n$ are also obtained via the eigendecomposition of $\tilde{\mathbf{Q}}$ in *step 2*. It is clear that any value of $l$ in (20) will uniquely derive the mode amplitudes $a_n$. However, using only one of these values to determine the mode amplitude will cause minor errors and decrease the accuracy of the calculation of $a_n$. Instead, the pseudoinverse approach is explored to solve these overdetermined equations, where the least-squares error is used. Specifically, (20) in matrix form can be expressed as

$$\mathbf{A}\mathbf{x} = \mathbf{b} \tag{21}$$

where $\mathbf{A}$ denotes the coefficient matrix with the size of $\tilde{N}L \times \tilde{N}$, $\mathbf{b}$ refers to the forcing term that is composed of the reduced snapshots, and $\mathbf{x}$ is the unknown mode amplitudes vector, which are defined as follows:

$$\mathbf{A} = \begin{bmatrix} \tilde{\mathbf{U}} \\ \tilde{\mathbf{U}}\boldsymbol{\Xi} \\ \cdots \\ \tilde{\mathbf{U}}\boldsymbol{\Xi}^{L-1} \end{bmatrix}, \quad \mathbf{x} = \begin{bmatrix} a_1 \\ a_2 \\ \cdots \\ a_{\tilde{N}} \end{bmatrix}, \quad \mathbf{b} = \begin{bmatrix} \tilde{\mathbf{d}}_1 \\ \tilde{\mathbf{d}}_2 \\ \cdots \\ \tilde{\mathbf{d}}_L \end{bmatrix} \tag{22}$$

where $\boldsymbol{\Xi}$ is a $\tilde{N} \times \tilde{N}$ diagonal matrix that is formed by the eigenvalues, $\xi$, in (20). It is clear that the mode amplitudes can be obtained by solving the over-determined equation shown in (21). In particular, the pseudoinverse of $\mathbf{A}$ is computed by the SVD method, which can be expressed as

$$\mathbf{A} = \mathbf{U_1}\mathbf{S_1}\mathbf{V_1}^H. \tag{23}$$

Substituting (23) into (21) and premultiplying the resulting equation by $\mathbf{V_1}\mathbf{S_1}^{-1}\mathbf{U_1}^H$, one can obtain

$$\mathbf{x} = \mathbf{V_1}\mathbf{S_1}^{-1}\mathbf{U_1}^H\mathbf{b}. \tag{24}$$

Thus, the mode amplitudes $a_n$ are calculated. Similar to the truncation in SVD, we define the threshold $\varepsilon_{\mathrm{DMD}}$ to determine $N$, which is given as

$$\frac{|a_N|}{\max(|a_n|)} < \varepsilon_{\mathrm{DMD}}. \tag{25}$$

Clearly, $\varepsilon_{\mathrm{DMD}}$ controls the number of linearly independent modes to be retained, namely $N$. Clearly, all the parameters in (13) are obtained merely from the calculation of the data matrix now, which means the expansion in the low-dimensional system is determined. To reconstruct the original HSI data, we premultiply (13) by the spatial SVD mode $\mathbf{U}$ according to (11). Finally, the expansion in (7) is obtained, and thereby the reconstruction of HSIs is achieved. Also, the pseudocode of DMD is depicted in Algorithm 1.

### *B. Cube Dynamic Mode Decomposition*

In the conventional DMD method, the horizontal and lateral dimension are reshaped into the one-dimensional spatial domain in advance. HSIs, however, are naturally represented by a three-order tensor. In this case, the conventional DMD method used to process matrix data sets needs to be modified to process higher-order tensors. Based on the fact that hyperspectral data has a natural feature of cube shape, we newly proposed CubeDMD to address this issue.

**Algorithm 1:** DMD.

**Input:** Hyperspectral data matrix: $\mathbf{D}$; the spectral interval: $\Delta\lambda$; DMD threshold: $\varepsilon_{\text{DMD}}$
**Output:** Spatial dynamic modes: $\mathbf{q}$; spectral patterns including damping rates: $\delta$ and frequencies: $\omega$; Reconstruction HSIs: $\mathbf{D}_{Rect}$

1: Split $\mathbf{D}$ into two adjacent matrices: $\mathbf{D}_1^{L-1}$ and $\mathbf{D}_2^{L}$;
2: Linear mapping assumption: $\mathbf{D}_2^L \simeq \mathbf{Q}\mathbf{D}_1^{L-1}$ (see (8));
3: Low-dimensional representation using SVD: $\tilde{\mathbf{d}}_l \simeq \sum_{n=1}^{\tilde{N}} a_n \tilde{\mathbf{q}}_n e^{(\delta_n + \mathrm{i}\omega_n)(l-1)\Delta\lambda}$;
4: Computation of damping rates $\delta_n$ and frequencies $\omega_n$: eigendecomposition of $\tilde{\mathbf{Q}}$;
5: Computation of the mode amplitudes: solving the overdetermined equation $\mathbf{A}\mathbf{x} = \mathbf{b}$;
6: **Return** $\mathbf{D}_{\textbf{Rect}}$: the low-rank representation of HSIs.

**Algorithm 2:** CubeDMD.

**Input:** Hyperspectral data tensor: $\mathcal{T}_{i_1,i_2,l}$; the spectral interval: $\Delta\lambda$; DMD threshold: $\varepsilon_{\text{DMD}}$
**Output:** Spatial dynamic modes in tensor form: $\mathcal{V}_{i_1,i_2,n}$; spectral patterns including damping rates: $\delta$ and frequencies: $\omega$; Reconstruction HSIs: $\mathcal{T}_{i_1,i_2,l_{Rect}}$

1: Implement HOSVD on $\mathcal{T}_{i_1,i_2,l}$: $\mathcal{T}_{i_1,i_2,l} = \sum_{n_1=1}^{N_1}\sum_{n_2=1}^{N_2}\sum_{n_3=1}^{N_3} \mathcal{S}_{n_1n_2n_3}\mathbf{U}^1_{n_1i_1}\mathbf{U}^2_{n_2i_2}\mathbf{U}^3_{n_3l}$;
2: Split $\mathcal{T}_{i_1,i_2,l}$ into rescaled core tensor $\tilde{\mathcal{S}}$ and the reduced snapshots $\tilde{\mathbf{U}}$ [see (29) and (30)];
3: Implement DMD on the reduced snapshots $\tilde{\mathbf{U}}$;
4: Computation of damping rates $\delta_n$ and frequencies $\omega_n$;
5: Computation of the mode amplitudes;
6: **Return** $\mathcal{T}_{i_1,i_2,l_{\textbf{Rect}}}$: the low-rank representation of HSIs in tensor form.

Similar to (7), the third-order hyperspectral image tensor shown in Fig. 1 could be expressed as follows:

$$\mathcal{T}_{i_1,i_2,l} = \sum_{n=1}^{N} a_n \mathcal{V}_{i_1,i_2,n} e^{(\delta_n + \mathrm{i}\omega_n)(l-1)\Delta\lambda} \tag{26}$$

where $\mathcal{V}_{i_1,i_2,n}$ refers to $n$th spatial mode tensor of order three. Obviously, unlike the conventional DMD method that encompasses $(i_1, i_2)$ in a single index, CubeDMD directly processes spatial snapshots on these two indexes. In this case, HOSVD is applied to replace the SVD approach implemented in the *step 1* for dimension reduction. The expansion of HOSVD is recalled here for convenience.

$$\mathcal{T}_{i_1,i_2,l} = \sum_{n_1=1}^{N_1}\sum_{n_2=1}^{N_2}\sum_{n_3=1}^{N_3} \mathcal{S}_{n_1n_2n_3}\mathbf{U}^1_{n_1i_1}\mathbf{U}^2_{n_2i_2}\mathbf{U}^3_{n_3l} \tag{27}$$

in terms of the core tensor $\mathcal{S}$ and the reduced snapshots along the horizontal, lateral, and spectral dimensions denoted as $\mathbf{U}^1_{n_1i_1}\mathbf{U}^2_{n_2i_2}$, and $\mathbf{U}^3_{n_3l}$, respectively. For convenience, expansion (27) is rewritten as

$$\mathcal{T}_{i_1,i_2,l} = \sum_{n_1=1}^{N_1}\sum_{n_2=1}^{N_2}\sum_{n_3=1}^{N_3} \tilde{\mathcal{S}}_{n_1n_2n_3}\tilde{\mathbf{U}}^3_{n_3l} \tag{28}$$

where $\tilde{\mathcal{S}}$ and $\tilde{\mathbf{U}}$ refer to the rescaled core tensor and the reduced snapshots, respectively, which are defined as

$$\tilde{\mathcal{S}}_{n_1n_2n_3} = \frac{1}{\xi^3_{n_3}}\sum_{n_1=1}^{N_1}\sum_{n_2=1}^{N_2}\sum_{n_3=1}^{N_3} \mathcal{S}_{n_1n_2n_3}\mathbf{U}^1_{n_1i_1}\mathbf{U}^2_{n_2i_2} \tag{29}$$

and

$$\tilde{\mathbf{U}}^3_{n_3l} = \xi^3_{n_3}\mathbf{U}^3_{n_3l} \tag{30}$$

respectively. Here, $\xi^3_{n_3}$ refers to the HOSVD singular values along the third dimension of the tensor $\mathcal{T}$. The column of reduced snapshots is given as $\tilde{\mathbf{U}}^3_{n_3l} = [\tilde{\mathbf{u}}_{n_31}, \tilde{\mathbf{u}}_{n_32}, \ldots, \tilde{\mathbf{u}}_{n_3l}, \ldots, \tilde{\mathbf{u}}_{n_3N}]$, where

$$\tilde{\mathbf{u}}_{n_3l} = \begin{bmatrix} \tilde{\mathbf{u}}_{1^{\frown}l} \\ \tilde{\mathbf{u}}_{2^{\frown}l} \\ \cdots \\ \tilde{\mathbf{u}}_{N_3l} \end{bmatrix}. \tag{31}$$

Next, proceeding with these reduced snapshots $\tilde{\mathbf{U}}^3_{n_3l}$ as we did in *steps 1, 2, and 3* described in Section III-A, we derive for the reduced snapshots the expansion, which can be expressed as

$$\tilde{\mathbf{u}}_{n_3l} = \sum_{n=1}^{N} a_n \tilde{\mathbf{v}}_{n_3n} e^{(\delta_n + \mathrm{i}\omega_n)(l-1)\Delta\lambda}. \tag{32}$$

Substituting (32) into (28), one can obtain

$$\mathcal{T}_{i_1,i_2,l} = \sum_{n=1}^{N} a_n \mathcal{V}_{i_1,i_2,n} e^{(\delta_n + \mathrm{i}\omega_n)(l-1)\Delta\lambda} \tag{33}$$

where

$$\mathcal{V}_{i_1,i_2,n} = \sum_{n_3=1}^{N_3} \tilde{\mathcal{S}}_{n_1n_2n_3}\tilde{\mathbf{v}}_{n_3n}. \tag{34}$$

Note that the parameters in (33), including the damping factors, frequencies, and the mode amplitude, are derived by the conventional DMD method in (32). The spatial mode in terms of tensor $\mathcal{V}$ is computed by the HOSVD and the conventional DMD by recombining the results of the HOSVD and the conventional DMD method, as shown in (34). Similarly, the pseudocode of CubeDMD is shown in Algorithm 2. Obviously, through CubeDMD, a tensor-based reduced-order expression of the HSIs is obtained in the two-dimensional spatial domain and the spectral domain.

## IV. Results

### A. Example 1: AVIRIS Hyperspectral Data

*1) Salinas Scene:* To verify the proposed approach, we first use the measured hyperspectral image data at the Salinas scene, which is collected by the Airborne Visible/Infrared Imaging Spectrometer (AVIRIS) sensor [56]–[58]. This hyperspectral image dataset is observed across 224 EM bands, and the number of horizontal and lateral pixels are 512 and 217, respectively, where the spatial resolution is about 3.7 m in each pixel. Thus, the tensor size of the AVIRIS data is $512 \times 217 \times 224$. Fig. 3 plots the AVIRIS HSIs with different EM bands. Obviously, pixels with different geomorphic features correspond to different responses of the EM waves, which is the significantly basic of

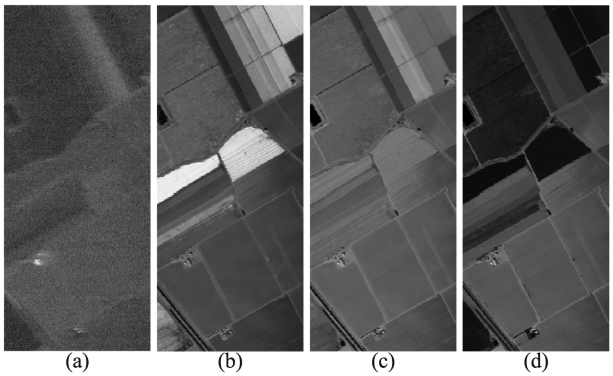


Fig. 3. Gray-scale images of AVIRIS hyperspectral data with the index of (a) 2, (b) 50, (c) 100, and (d) 200 EM bands.

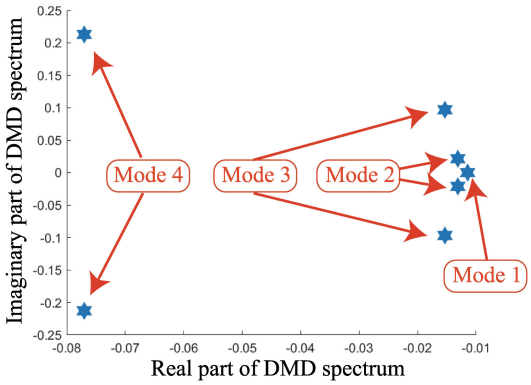


Fig. 4. Visualization of the DMD spectrum.

landform classification. In this case, the spectral distribution of each pixel is the additional advantage of HSIs, so it is of great consequence to represent the spectral distribution of pixels accurately in the low-rank reconstruction. In addition, it can be clearly seen that Fig. 3(a) is very blurry, which is caused by the existence of noise that is unavoidable in the hyperspectral collection. In specific, the quality of hyperspectral data may be substantially downgraded by several undesirable noise sources, such as atmospheric effects and the degradation mechanisms associated with the measurement process. Interestingly, the proposed DMD-based framework takes advantage of the SVD and HOSVD approaches, which can reduce the interference of noise and thereby recover the poor quality HSIs. This denoising effect will be demonstrated in the following reconstruction part.

*2) Decomposition:* To further illustrate the process of the proposed DMD-based approach, the intermediate decomposition results, namely the DMD spectrum and the extracted DMD modes, are presented. Hereinto, $\varepsilon_{\text{DMD}}$ is set to $1 \times 10^{-2}$, and seven eigenvalues are retained in the decomposition. Fig. 4 plots the DMD spectrum that shows the distribution of the eigenvalues. Notably, HSIs here are represented in the real-valued analytic space. Hence, a pair of eigenvalues with the same real part corresponds to one spatial DMD mode, except for the case where the imaginary part of the eigenvalues is 0. This ensures that the reconstructed hyperspectral data is still in the real analytic space. In this case of Fig. 4, four spatial DMD modes can be extracted

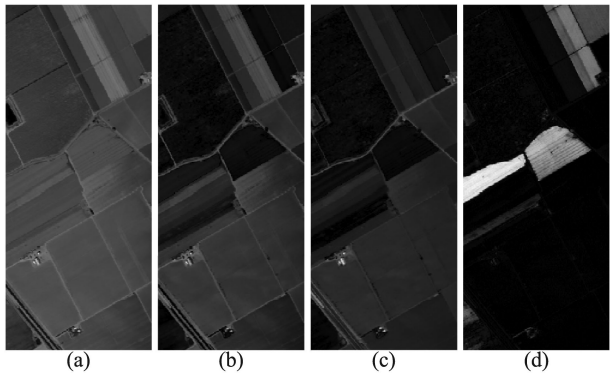


Fig. 5. Visualization of the DMD modes.

and plotted in Fig. 5. Visually, these DMD modes are very similar to the spatial distribution of the original hyperspectral data shown in Fig. 3. According to (7), the eigenvalues in the DMD spectrum also determine the change of each corresponding mode as the EM band index increases. In addition to the intuitive feature extraction shown in Fig. 5, quantitative analysis is performed to further demonstrate the accuracy of the reconstruction based on these decomposed results in the following performance part.

*3) Reconstruction:* Based on the aforementioned decomposed results, the reconstruction can be obtained according to (7). Hereinto, the SVD-based methods, namely the traditional SVD for the matrix form of HSIs and the HOSVD for the tensor form of HSIs, respectively, are also considered for the comparison. Both $\varepsilon_{\text{SVD}}$ and $\varepsilon_{\text{DMD}}$ are set to $1 \times 10^{-4}$. Fig. 6 presents the visual comparison of partial reconstruction results, including four EM bands shown in Fig. 3. For each subgraph, the first row, respectively, shows the approximate reconstruction results obtained by four methods, namely SVD, HOSVD, DMD, and CubeDMD. The second row presents the spatial distribution of residual between the original hyperspectral data and reconstructed results. From Fig. 6(a), we can see that the noise at band #2 is greatly removed in the reconstruction results obtained in all four methods. This is because these four methods take advantage of the truncation step. It is worth noting that, compared with the SVD-based methods, the DMD-based approaches have a larger residual near the end of the band. This is because, unlike SVD that uses the spectral mode $\mathbf{V}$ same as the original spectral dimension to represent the HSIs, DMD further compresses the hyperspectral data by using the eigenvalues, of which number is lower than the spectral dimension. Then, errors will occur at the end of the EM band number. However, as shown in Fig. 6(b) and (c), it can be easily observed that the proposed DMD approach has the best reconstruction effect with the least residual. Hence, we can conclude that the proposed DMD method can represent the HSIs with noise removal and acceptable spatial distribution accuracy.

In addition, the reconstructed spectral distributions are visualized to demonstrate the effectiveness of the proposed approach. We randomly select nine pixels and plot their corresponding normalized amplitude distribution versus the index of EM bands

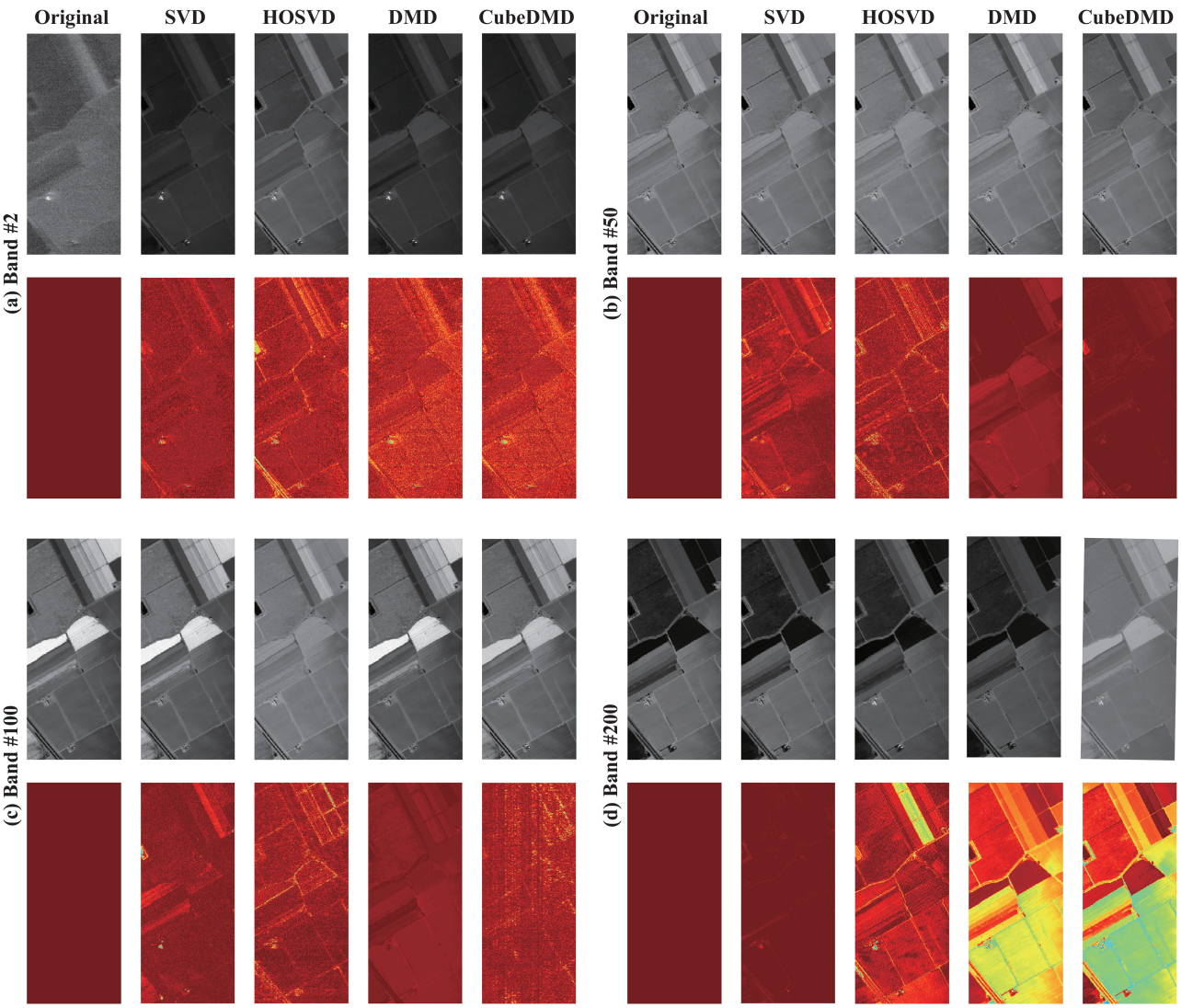


Fig. 6. Gray images of AVIRIS hyperspectral data with the index of (a) 2, (b) 50, (c) 100, and (d) 200 EM bands. The first column of each subgraph, from left to right, is the original visual image, the reconstructed results obtained by SVD, HOSVD, DMD, and the CubeDMD. The corresponding color images below refer to the residual spatial distribution between the reconstructed images and their ground truths.

in Fig. 7. Clearly, although there are some errors near the end of EM bands, the overall amplitude distribution can be well reconstructed, especially at the middle indices of EM bands with high intensity. Hence, the DMD method can well represent the spectral distribution of hyperspectral pixels.

*4) Performance:* To further verify the proposed method, we quantitatively analyze the reconstruction results obtained by the DMD-based framework. Herein, the mean peak signal-to-noise ratio (PSNR) [6], [59] and mean spectral angle mapper (SAM) [59] are adopted as the reconstruction evaluation measures. In specific, PSNR in dB is defined as

$$\begin{aligned}\mathrm{PSNR} &= 10 \cdot \log_{10}\left(\frac{\mathrm{MAXI}^2}{\mathrm{MSE}}\right) \\ &= 20 \cdot \log_{10}\left(\frac{\mathrm{MAXI}}{\sqrt{\mathrm{MSE}}}\right). \end{aligned} \tag{35}$$

Here, MAXI refers to the maximum possible pixel intensity of the image, and MSE denotes the mean squared error, which is given as

$$\mathrm{MSE} = \frac{1}{OP}\sum_{i_1=1}^{O}\sum_{i_2=1}^{P}[Orig(i_1,i_2) - Rect(i_1,i_2)]^2 \tag{36}$$

where $O$ and $P$, respectively, denote the total number of pixels in the horizontal and lateral dimension, $Orig$ means the original images, and $Rect$ means the reconstructed images. Table I shows

TABLE I
PSNR VALUES OF THE HYPERSPECTRAL IMAGES SHOWN IN FIG. 3

| Number of EM bands | PSNR | | | |
|---|---|---|---|---|
| | SVD | HOSVD | DMD | CubeDMD |
| 2 | 22.07 | 22.23 | **27.43** | 26.30 |
| 50 | 21.31 | 21.17 | **43.70** | 43.37 |
| 100 | 29.69 | 28.90 | **43.72** | 42.71 |
| 200 | **17.13** | 17.12 | 14.97 | 14.96 |
| Average | 26.47 | 26.29 | **31.47** | 31.19 |

The bold entities represents the best result among the four methods.

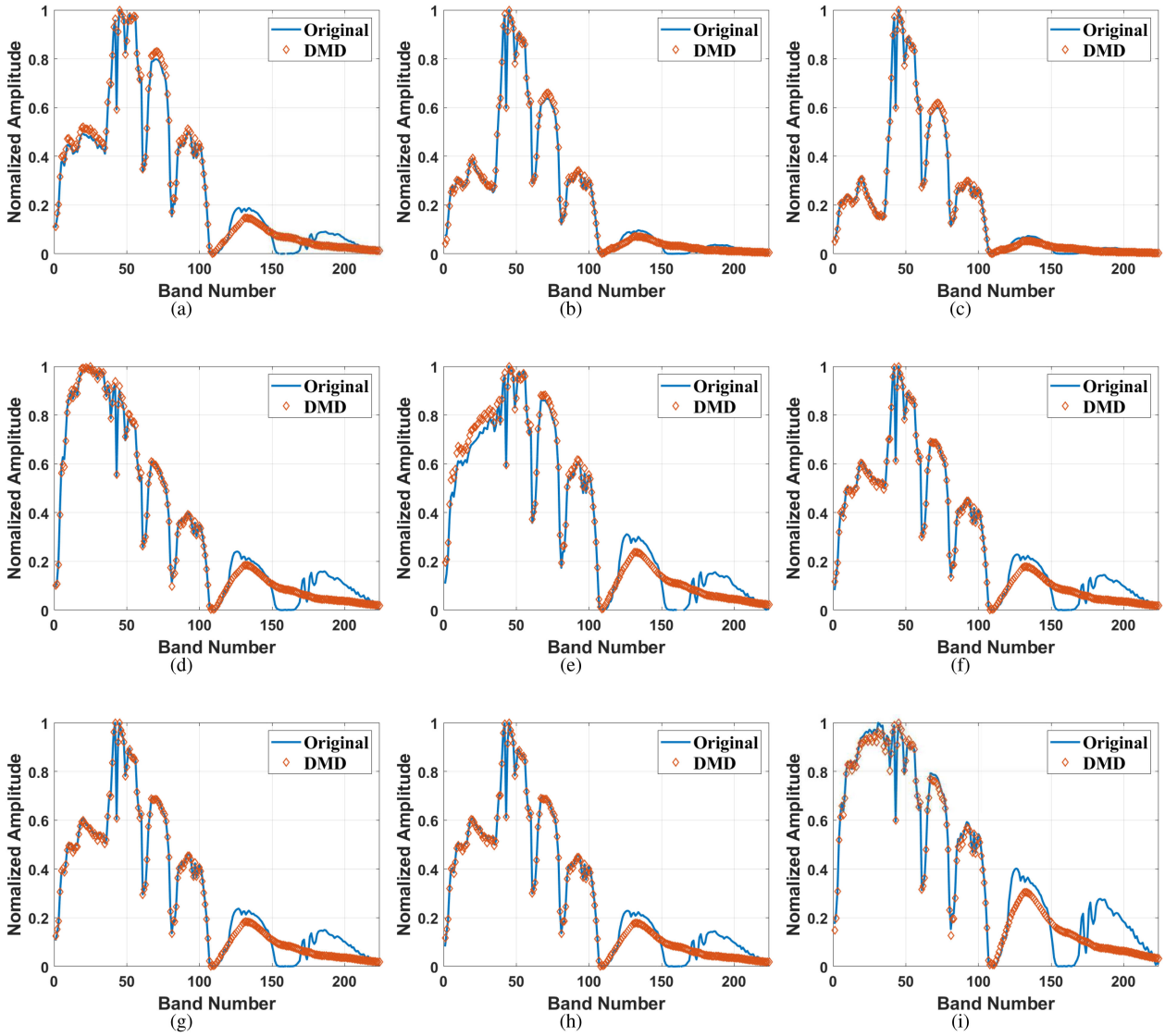


Fig. 7. Normalized amplitude distribution versus the index of EM bands at (a) #100, (b) #1000, (c) #1500, (d) #3000, (e) #6500, (f) #7500, (g) #30 000, (h) #75 000, and (i) #90 400 pixel.

the calculated PSNR values of the hyperspectral images shown in Fig. 3. Clearly, while the reconstruction obtained by DMD at the 200th band is not the best, the DMD reconstruction result has the largest PSNR value in the remaining bands. By averaging the PSNRs of all bands, shown in the last row of the Table I, it is also proved that DMD is the most effective representation method. Besides, Fig. 8 plots PSNR versus the index of EM bands. It also can be seen that the DMD-based methods are better than SVD-based methods in most EM bands.

In addition, the SAM is also calculated for further verification. SAM is usually used to measure spectral similarity by calculating the angle between two spectral vectors of the original and reconstructed images. Mathematically, the SAM index at the $i$th pixel can be expressed as follows:

$$SAM\left(\mathbf{x}_i, \hat{\mathbf{x}}_i\right) = \arccos\left(\frac{\mathbf{x}_i^T \hat{\mathbf{x}}_i}{\|\mathbf{x}_i\|_2 \|\hat{\mathbf{x}}_i\|_2}\right). \quad (37)$$

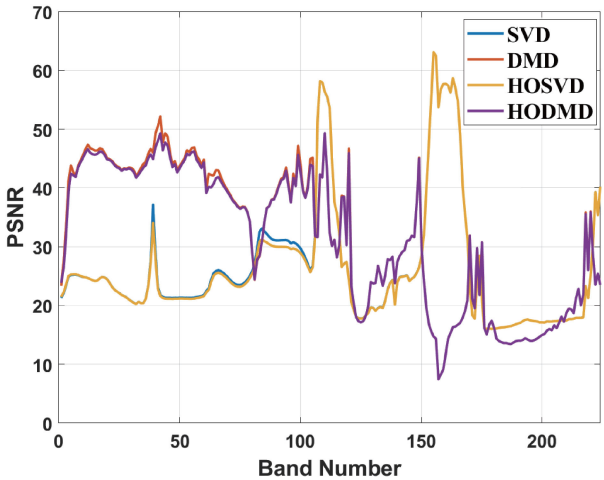


Fig. 8. PSNR versus the index of EM bands with AVIRIS hyperspectral data.

TABLE II
SAM VALUES OF THE SPECTRAL VECTORS SHOWN IN FIG. 7

| Index of pixels | SAM | | | |
|---|---|---|---|---|
| | SVD | HOSVD | DMD | CubeDMD |
| 100 | 0.0773 | 0.0782 | **0.0746** | 0.0756 |
| 1000 | 0.0491 | 0.0491 | **0.0455** | **0.0455** |
| 1500 | 0.3256 | 0.3263 | **0.0373** | 0.0374 |
| 3000 | 0.1420 | 0.1453 | **0.0938** | 0.0939 |
| 6500 | 0.1107 | 0.1107 | **0.1081** | 0.1096 |
| 7500 | **0.0321** | 0.0328 | 0.1010 | 0.1017 |
| 30000 | **0.0365** | 0.0439 | 0.1045 | 0.1050 |
| 75000 | 0.2041 | 0.2043 | **0.1337** | 0.1347 |
| 90400 | 0.2305 | 0.2305 | **0.1434** | 0.1438 |
| Average | 0.2206 | 0.2219 | **0.1037** | 0.1042 |

The bold entities represents the best result among the four methods.

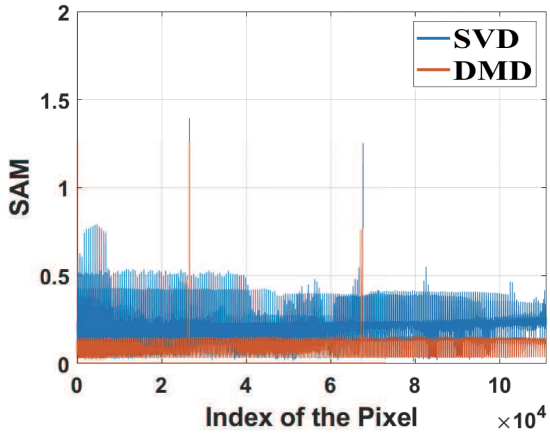


Fig. 9. SAM versus the index of pixels with AVIRIS hyperspectral data.

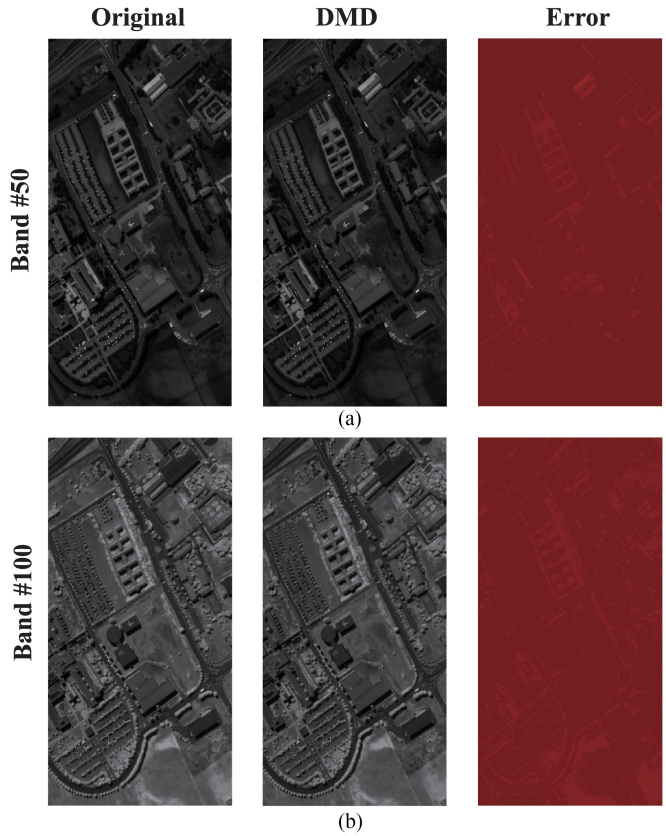


Fig. 10. Gray images of ROSIS hyperspectral data with the index of (a) 50 and (b) 100 EM bands. The first column of each subgraph, from left to right, is the original visual image, the reconstructed results obtained DMD, and the residual spatial distribution.

The SAM values of the spectral vectors plotted in Fig. 7 are computed and shown in Table II. It is clear that the spectrum vector obtained by DMD has the smallest SAM value on most pixels. The average value of SAM of all spatial pixels is presented in the last row of Table II. We can see that the DMD reconstruction method has the smallest SAM value. Also, SAM versus the index of pixel is plotted in Fig. 9. It can be easily seen that the SAM value obtained from DMD is smaller than that obtained from the SVD approach. Hence, due to the larger PSNR or small SAM of the DMD approach, we can conclude that the proposed DMD-based framework outperforms the SVD-based one on the reconstruction accuracy of HSIs.

### *B. Example 2: ROSIS Hyperspectral Data*

In this case, we analyze the HSIs data obtained by the ROSIS sensor for further validation. Herein, we use the scene of the Pavia University [60]. A total of 103 EM bands are used in this observation. The spatial dimension is $610 \times 340$, and the geometric resolution is 1.3 m, where the corresponding tensor has the size of $610 \times 340 \times 130$.

Fig. 10 shows the reconstruction result obtained from the DMD method. The $\varepsilon_{\text{DMD}}$ is set to $1 \times 10^{-4}$. Obviously, the reconstructed images at band #50 and #100 have a good agreement with the original ones. Besides, the corresponding residual spatial distribution is plotted in the last column. We can see that the error between the reconstruction and the original images is tiny. Moreover, the obtained spectral distributions are shown to illustrate the effectiveness of the proposed approach. Specifically, six pixels are randomly chosen. Their normalized amplitude distribution versus the index of EM bands is plotted in Fig. 11. It can be seen that the spectral distribution of hyperspectral pixels obtained from the DMD method shows high consistency with the original ones. Hence, the DMD method can satisfactorily describe the spectral distribution of HSIs.

To further validate the proposed method, the PSNR and SAM are also investigated in this case. Fig. 12 shows the PSNR versus the index of EM bands. It is clear that compared with other methods, the DMD method achieves the largest PNSR value in most bands, so it has the best reconstruction results. Moreover, the SAM of each pixel is calculated and plotted in Fig. 13. Obviously, the SAM computed based on the DMD method is generally smaller than that extracted from SVD at each pixel. Consequently, the proposed method has better performance than the SVD-based method, which is consistent with the conclusion drawn from the first example. Additionally, it is worth noting that the proposed method provides a low-rank representation for HSIs, which could be utilized in the classification of hyperspectral data in the future.

For further verification, four tensor-based dimensionality reduction methods are analyzed using ROSIS hyperspectral data, namely hierarchical Tucker (HT) decomposition [61], tensor-train (TT) decomposition [62], HOSVD, and the proposed

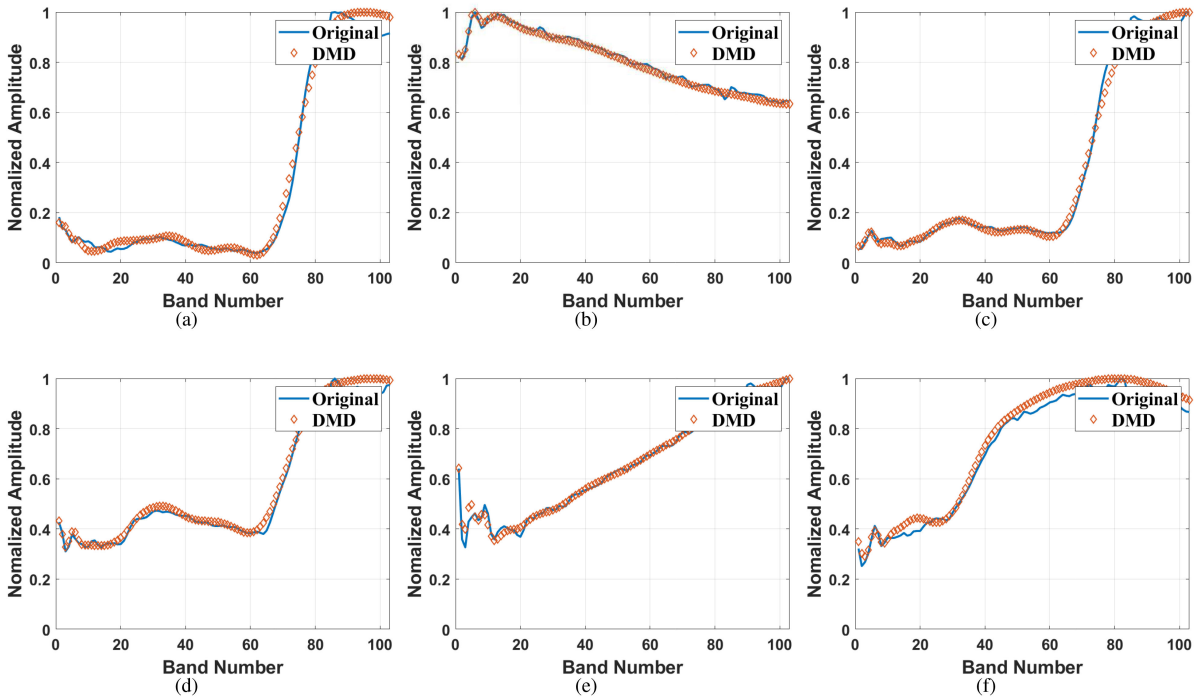


Fig. 11. Normalized amplitude distribution versus the index of EM bands at (a) #1, (b) #1000, (c) #5000, (d) #80 000, (e) #70 000, and (f) #160 000 pixel.

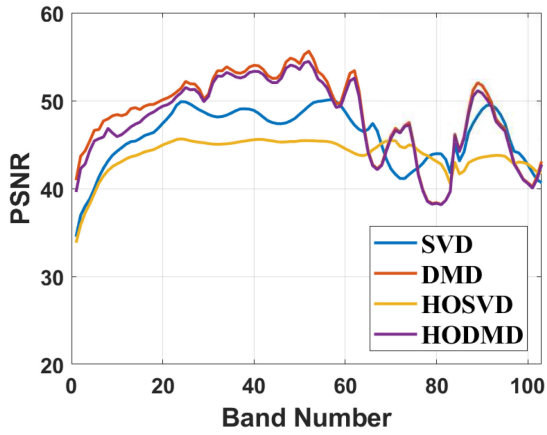


Fig. 12. PSNR versus the index of EM bands with ROSIS hyperspectral data.

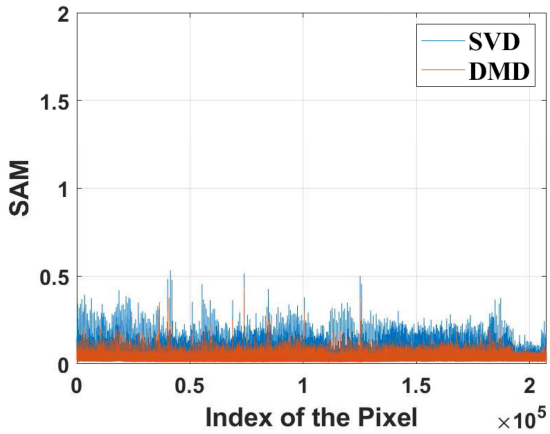


Fig. 13. SAM versus the index of pixels with ROSIS hyperspectral data.

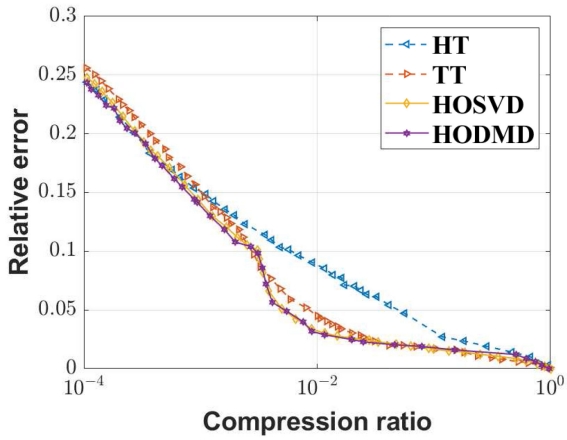


Fig. 14. Comparison results. Relative error versus the compression ratio of HT, TT, HOSVD, and CubeDMD.

CubeDMD. The comparison result is plotted in Fig. 14. Because the same bytes are used here to represent the original data and the reconstructed data, the compression ratio is computed by the ratio of reconstructed data and original data. And the relative error is defined as

$$\text{Relative error} = \frac{\|Orig - Rect\|}{\|Orig\|}. \tag{38}$$

As shown in Fig. 14, we can see that the HOSVD and CubeDMD offer very similar performance for low compression ratio (its value is below $10^{-2}$). And the TT method achieves the best performance at extremely low compression ratios, where its value is below $10^{-1}$. For high compression ratios where its value is larger than $10^{-2}$, the proposed CubeDMD method outperforms other methods. Additionally, the computational

TABLE III
COMPUTATIONAL COMPLEXITY OF EACH METHOD USED IN FIG. 14

| Method | HT | TT | HOSVD | CubeDMD |
|---|---|---|---|---|
| Computational complexity | $\mathcal{O}\left(3IR+3R^3\right)$ | $\mathcal{O}\left(3I^2R^2\right)$ | $\mathcal{O}\left(3IR+R^3\right)$ | $\mathcal{O}\left(3IR+2R^3\right)$ |

complexity of each method is analyzed [63] and listed in Table III. Herein, we define $I=\max\{I_1,I_2,I_3\}$, and $R$ means the upper bound on the ranks of these tensor decompositions approach, namely $R=\max\{R_1,R_2,R_3\}$. Notably, compared with HOSVD, CubeDMD needs to further solve the $\mathbf{Ax}=\mathbf{b}$ problem based on the spectral mode matrix, so the computational complexity increases by one more cubic complexity.

## V. CONCLUSION

To sum up, we demonstrated the DMD-based approach to compress and reconstruct the HSIs. The proposed start-of-the-art data-driven approach deals with the HSIs as a spatial-spectral correlated real signal. It decomposes hyperspectral data into the DMD spatial modes and corresponding spectral patterns, which can be adopted to reconstruct the HSIs. Furthermore, according to the natural property that hyperspectral data is a third-order tensor, we proposed the CubeDMD method for dimensionality reduction of the horizontal and vertical coordinates in the spatial domain. The proposed DMD-based framework was validated via the measured hyperspectral data at the Salinas scene and Pavia University. Compared with the traditional SVD-based method, although the proposed method requires more computation steps, it can reconstruct more realistic HSIs not only in the spatial domain but also in the spectral domain. Therefore, our article offers a practical low-rank representation technique for HSIs.

## ACKNOWLEDGMENT

The authors are grateful to Jet Propulsion Laboratory and Telecommunications and Remote Sensing Laboratory for offering the open source of the AVIRIS and Pavia University hyperspectral image datasets.

## REFERENCES

[1] J. M. Haut, M. E. Paoletti, J. Plaza, J. Li, and A. Plaza, "Active learning with convolutional neural networks for hyperspectral image classification using a new Bayesian approach," *IEEE Trans. Geosci. Remote Sens.*, vol. 56, no. 11, pp. 6440–6461, Nov. 2018.

[2] P. Ghamisi *et al.*, "Advances in hyperspectral image and signal processing: A comprehensive overview of the state of the art," *IEEE Geosci. Remote Sens. Mag.*, vol. 5, no. 4, pp. 37–78, Dec. 2017.

[3] Z. He, K. Xia, T. Li, B. Zu, Z. Yin, and J. Zhang, "A constrained graph-based semi-supervised algorithm combined with particle cooperation and competition for hyperspectral image classification," *Remote Sens.*, vol. 13, no. 2, 2021, Art. no. 193.

[4] A. Sha, B. Wang, X. Wu, and L. Zhang, "Semisupervised classification for hyperspectral images using graph attention networks," *IEEE Geosci. Remote. Sens. Lett.*, vol. 18, no. 1, pp. 157–161, Jan. 2020.

[5] H. V. Nguyen, M. O. Ulfarsson, and J. R. Sveinsson, "Sure based convolutional neural networks for hyperspectral image denoising," in *Proc. IEEE Int. Geosci. Remote Sens. Symp.*, 2020, pp. 1784–1787.

[6] Y. Xu, Z. Wu, J. Chanussot, and Z. Wei, "Joint reconstruction and anomaly detection from compressive hyperspectral images using Mahalanobis distance-regularized tensor RPCA," *IEEE Trans. Geosci. Remote Sens.*, vol. 56, no. 5, pp. 2919–2930, May 2018.

[7] M. T. Zeegers, D. M. Pelt, T. van Leeuwen, R. van Liere, and K. J. Batenburg, "Task-driven learned hyperspectral data reduction using end-to-end supervised deep learning," *J. Imag.*, vol. 6, no. 12, 2020, Art. no. 132.

[8] Y. Wang, K. Li, L. Xu, Q. Wei, F. Wang, and Y. Chen, "A depthwise separable fully convolutional ResNet with ConvCRF for semisupervised hyperspectral image classification," *IEEE J. Sel. Topics Appl. Earth Observ. Remote Sens.*, vol. 14, pp. 4621–4632, 2021.

[9] S. Lim, K. H. Sohn, and C. Lee, "Principal component analysis for compression of hyperspectral images," in *Proc. IEEE Int. Geosci. Remote Sens. Symp.*, 2001, vol. 1, pp. 97–99.

[10] A. A. Green, M. Berman, P. Switzer, and M. D. Craig, "A transformation for ordering multispectral data in terms of image quality with implications for noise removal," *IEEE Trans. Geosci. Remote Sens.*, vol. 26, no. 1, pp. 65–74, Jan. 1988.

[11] H. Du, H. Qi, X. Wang, R. Ramanath, and W. E. Snyder, "Band selection using independent component analysis for hyperspectral image processing," in *Proc. 32nd Appl. Imagery Pattern Recognit. Workshop*, 2003, pp. 93–98.

[12] J. Zhang, J. Erway, X. Hu, Q. Zhang, and R. Plemmons, "Randomized SVD methods in hyperspectral imaging," *J. Elect. Comput. Eng.*, vol. 2012, 2012, Art. no. 409357.

[13] F. Zhong, J. Zhang, and D. Li, "Discriminant locality preserving projections based on l1-norm maximization," *IEEE Trans. Neural Netw. Learn. Syst.*, vol. 25, no. 11, pp. 2065–2074, Nov. 2014.

[14] S. Wang and W. Zhu, "Sparse graph embedding unsupervised feature selection," *IEEE Trans. Syst. Man Cybern. Syst.*, vol. 48, no. 3, pp. 329–341, Mar. 2018.

[15] G. Shi, H. Huang, and L. Wang, "Unsupervised dimensionality reduction for hyperspectral imagery via local geometric structure feature learning," *IEEE Geosci. Remote. Sens. Lett.*, vol. 17, no. 8, pp. 1425–1429, Aug. 2020.

[16] J. Jiang, J. Ma, C. Chen, Z. Wang, Z. Cai, and L. Wang, "SuperPCA: A superpixelwise PCA approach for unsupervised feature extraction of hyperspectral imagery," *IEEE Trans. Geosci. Remote Sens.*, vol. 56, no. 8, pp. 4581–4593, Aug. 2018.

[17] J. Song, J.-H. Jeong, D.-S. Park, H.-H. Kim, D.-C. Seo, and J. C. Ye, "Unsupervised denoising for satellite imagery using wavelet directional cycle-GAN," *IEEE Trans. Geosci. Remote Sens.*, vol. 59, no. 8, pp. 6823–6839, Aug. 2021.

[18] K. T. Shahid and I. D. Schizas, "Unsupervised hyperspectral unmixing via nonlinear autoencoders," *IEEE Trans. Geosci. Remote Sens.*, vol. 60, 2022, Art. no. 5506513.

[19] N. Khattab, S. Rashwan, H. M. Ebied, W. Sheta, H. Shedeed, and M. F. Tolba, "Unsupervised spectral-spatial multiscale feature learning framework for hyperspectral image classification based on multiple kernel self-organizing maps," *J. Appl. Remote Sens.*, vol. 14, no. 4, 2020, Art. no. 046503.

[20] J. Li, J. M. Bioucas-Dias, and A. Plaza, "Spectral-spatial hyperspectral image segmentation using subspace multinomial logistic regression and Markov random fields," *IEEE Trans. Geosci. Remote Sens.*, vol. 50, no. 3, pp. 809–823, Mar. 2012.

[21] F. Cao, Z. Yang, X. Hong, Y. Cheng, Y. Huang, and J. Lv, "Supervised dimensionality reduction of hyperspectral imagery via local and global sparse representation," *IEEE J. Sel. Topics Appl. Earth Observ. Remote Sens.*, vol. 14, pp. 3860–3874, 2021.

[22] G. Camps-Valls, T. V. B. Marsheva, and D. Zhou, "Semi-supervised graph-based hyperspectral image classification," *IEEE Trans. Geosci. Remote Sens.*, vol. 45, no. 10, pp. 3044–3054, Oct. 2007.

[23] L. Bruzzone, M. Chi, and M. Marconcini, "A novel transductive SVM for semisupervised classification of remote-sensing images," *IEEE Trans. Geosci. Remote Sens.*, vol. 44, no. 11, pp. 3363–3373, Nov. 2006.

[24] J. Li, J. M. Bioucas-Dias, and A. Plaza, "Semisupervised hyperspectral image segmentation using multinomial logistic regression with active learning," *IEEE Trans. Geosci. Remote Sens.*, vol. 48, no. 11, pp. 4085–4098, Nov. 2010.

[25] F. He, F. Nie, R. Wang, W. Jia, F. Zhang, and X. Li, "Semisupervised band selection with graph optimization for hyperspectral image classification," *IEEE Trans. Geosci. Remote Sens.*, vol. 59, no. 12, pp. 10298–10311, Dec. 2021.

[26] A. Zare, A. Ozdemir, M. A. Iwen, and S. Aviyente, "Extension of PCA to higher order data structures: An introduction to tensors, tensor decompositions, and tensor PCA," *Proc. IEEE*, vol. 106, no. 8, pp. 1341–1358, Aug. 2018.
[27] H. Li and L. Zhang, "A hybrid automatic endmember extraction algorithm based on a local window," *IEEE Trans. Geosci. Remote Sens.*, vol. 49, no. 11, pp. 4223–4238, Nov. 2011.
[28] J. An, J. Lei, Y. Song, X. Zhang, and J. Guo, "Tensor based multiscale low rank decomposition for hyperspectral images dimensionality reduction," *Remote Sens.*, vol. 11, no. 12, 2019, Art. no. 1485.
[29] F. Zhou and Z. Chen, "Hyperspectral image change detection by self-supervised tensor network," in *Proc. IEEE Int. Geosci. Remote Sens. Symp.*, 2020, pp. 2527–2530.
[30] K. Makantasis, A. Georgogiannis, A. Voulodimos, I. Georgoulas, A. Doulamis, and N. Doulamis, "Rank-R FNN: A tensor-based learning model for high-order data classification," *IEEE Access*, vol. 9, pp. 58609–58620, 2021.
[31] Y. Gao, X. Wang, Y. Cheng, and Z. J. Wang, "Dimensionality reduction for hyperspectral data based on class-aware tensor neighborhood graph and patch alignment," *IEEE Trans. Neural Netw. Learn. Syst.*, vol. 26, no. 8, pp. 1582–1593, Aug. 2015.
[32] J.-Y. Yang, H.-C. Li, Z.-C. Li, and T.-Y. Ma, "Spatial-spectral tensor graph convolutional network for hyperspectral image classification," in *Proc. IEEE Int. Geosci. Remote Sens. Symp.*, 2021, pp. 2222–2225.
[33] B. Feng and J. Wang, "Hyperspectral image dimension reduction using weight modified tensor-patch-based methods," *IEEE J. Sel. Topics Appl. Earth Observ. Remote Sens.*, vol. 13, pp. 3367–3380, 2020.
[34] F. Ye and Z. Chen, "Semisupervised classification based on tensor convolutional neural network for hyperspectral images," *J. Phys. Conf. Ser.*, vol. 1880, no. 1, 2021, Art. no. 012023.
[35] Z. Cao, X. Li, and L. Zhao, "Semisupervised hyperspectral imagery classification based on a three-dimensional convolutional adversarial autoencoder model with low sample requirements," *J. Appl. Remote Sens.*, vol. 14, no. 2, 2020, Art. no. 024522.
[36] P. Megha, V. Sowmya, and K. Soman, "Effect of dynamic mode decomposition-based dimension reduction technique on hyperspectral image classification," in *Computational Signal Processing and Analysis*, Berlin, Germany: Springer, 2018, pp. 89–99.
[37] C. Prévost, K. Usevich, P. Comon, and D. Brie, "Hyperspectral super-resolution with coupled tucker approximation: Recoverability and SVD-based algorithms," *IEEE Trans. Signal Process.*, vol. 68, pp. 931–946, 2020.
[38] Y. Ma, Y. Zhang, X. Mei, X. Dai, and J. Ma, "Multifeature-based discriminative label consistent K-SVD for hyperspectral image classification," *IEEE J. Sel. Topics Appl. Earth Observ. Remote Sens.*, vol. 12, no. 12, pp. 4995–5008, Dec. 2019.
[39] Z. Wang, J. Liu, and J.-H. Xue, "Joint sparse model-based discriminative k-SVD for hyperspectral image classification," *Signal Process.*, vol. 133, pp. 144–155, 2017.
[40] T. G. Kolda and B. W. Bader, "Tensor decompositions and applications," *SIAM Rev.*, vol. 51, no. 3, pp. 455–500, 2009.
[41] L. R. Tucker, "Some mathematical notes on three-mode factor analysis," *Psychometrika*, vol. 31, no. 3, pp. 279–311, 1966.
[42] L. De Lathauwer, B. De Moor, and J. Vandewalle, "A multilinear singular value decomposition," *SIAM J. Matrix Anal. Appl.*, vol. 21, no. 4, pp. 1253–1278, 2000.
[43] L. De Lathauwer, B. De Moor, and J. Vandewalle, "On the best rank 1 and rank (r1, r2,..., rn) approximation of higher-order tensors," *SIAM J. Matrix Anal. Appl.*, vol. 21, no. 4, pp. 1324–1342, 2000.
[44] N. Cheng, H. Huang, L. Zhang, and L. Wang, "Snapshot hyperspectral imaging based on weighted high-order singular value regularization," in *Proc. 25th Int. Conf. Pattern Recognit.*, 2021, pp. 1267–1274.
[45] C. Zeng and M. K. Ng, "Decompositions of third-order tensors: HOSVD, T-SVD, and beyond," *Numer. Linear Algebra Appl.*, vol. 27, no. 3, 2020, Art. no. e2290.
[46] L. Wang, W. S. H. Di Xiao, X. Y. Wu, and L. Chen, "A modified higher-order singular value decomposition framework with adaptive multilinear tensor rank approximation for three-dimensional magnetic resonance Rician noise removal," *Front. Oncol.*, vol. 10, 2020, Art. no. 1640.
[47] P. J. Schmid, "Dynamic mode decomposition of numerical and experimental data," *J. Fluid Mechan.*, vol. 656, pp. 5–28, 2010.
[48] Y. Zhang, M. L. Chen, and L. Jiang, "Extraction of the characteristics of vortex beams with a partial receiving aperture at arbitrary locations," *J. Opt.*, vol. 23, no. 8, 2021, Art. no. 085601.
[49] Y. Zhang and L. Jiang, "A novel demultiplexing scheme for vortex beams in radio communication systems," *IEEE Trans. Veh. Technol.*, vol. 70, no. 7, pp. 7243–7248, Jul. 2021.
[50] Y. Zhang, M. L. Chen, and L. J. Jiang, "Analysis of electromagnetic vortex beams using modified dynamic mode decomposition in spatial angular domain," *Opt. Exp.*, vol. 27, no. 20, pp. 27702–27711, 2019.
[51] E. Barocio, B. C. Pal, N. F. Thornhill, and A. R. Messina, "A dynamic mode decomposition framework for global power system oscillation analysis," *IEEE Trans. Power Syst.*, vol. 30, no. 6, pp. 2902–2912, Nov. 2015.
[52] Y. Zhang, L. Jiang, and H. T. Ewe, "A novel data-driven modeling method for the spatial-temporal correlated complex sea clutter," *IEEE Trans. Geosci. Remote Sens.*, vol. 60, Jul. 2021, Art. no. 5104211.
[53] Y. Zhang and L. Jiang, "A novel data-driven scheme for the ship wake identification on the 2-D dynamic sea surface," *IEEE Access*, vol. 8, pp. 69593–69600, 2020.
[54] S. L. Brunton, B. W. Brunton, J. L. Proctor, E. Kaiser, and J. N. Kutz, "Chaos as an intermittently forced linear system," *Nature Commun.*, vol. 8, no. 1, pp. 1–9, 2017.
[55] E. D. Rainville, P. E. Bedient, and R. E. Bedient, *Elementary Differential Equations*, vol. 10. New York, NY, USA: Macmillan, 1964.
[56] G. Vane, R. O. Green, T. G. Chrien, H. T. Enmark, E. G. Hansen, and W. M. Porter, "The airborne visible/infrared imaging spectrometer (AVIRIS)," *Remote Sens. Environ.*, vol. 44, no. 2, pp. 127–143, 1993.
[57] D. R. Thompson *et al.*, "Rapid spectral cloud screening onboard aircraft and spacecraft," *IEEE Trans. Geosci. Remote Sens.*, vol. 52, no. 11, pp. 6779–6792, Nov. 2014.
[58] A. K. Thorpe, D. A. Roberts, E. S. Bradley, C. C. Funk, P. E. Dennison, and I. Leifer, "High resolution mapping of methane emissions from marine and terrestrial sources using a cluster-tuned matched filter technique and imaging spectrometry," *Remote Sens. Environ.*, vol. 134, pp. 305–318, 2013.
[59] Y. Peng, D. Meng, Z. Xu, C. Gao, Y. Yang, and B. Zhang, "Decomposable nonlocal tensor dictionary learning for multispectral image denoising," in *Proc. IEEE Conf. Comput. Vis. Pattern Recognit.*, 2014, pp. 2949–2956.
[60] P. Gamba, "Telecommunications and remote sensing laboratory," Accessed: Nov. 15, 2021. [Online]. Available: http://tlclab.unipv.it/
[61] J. Ballani, L. Grasedyck, and M. Kluge, "Black box approximation of tensors in hierarchical tucker format," *Linear Algebra Appl.*, vol. 438, no. 2, pp. 639–657, 2013.
[62] I. V. Oseledets, "Tensor-train decomposition," *SIAM J. Sci. Comput.*, vol. 33, no. 5, pp. 2295–2317, 2011.
[63] A. Cichocki, N. Lee, I. Oseledets, A.-H. Phan, Q. Zhao, and D.P. Mandic, "Tensor networks for dimensionality reduction and large-scale optimization: Part 1 low-rank tensor decompositions," *Found. Trends Mach. Learn.*, vol. 9, no. 4-5, pp 249–429, 2016.

**Yanming Zhang** (Student Member, IEEE) received the B.Eng. degree in electrical engineering from the China University of Mining and Technology, Xuzhou, China, in 2015, the M.S. degree in electrical engineering from Southeast University, Nanjing, China, in 2018, and the Ph.D. degree in electrical engineering from the University of Hong Kong, Hong Kong, China, in 2021.

Since 2022, he has been a Postdoctoral Researcher with the Department of Electrical and Electronic Engineering, University of Hong Kong. His research interests include computational electromagnetics, data-driven methods, and quantum algorithms.

Dr. Zhang was a recipient of Merit Prize for the 21st IEEE (HK) AP/MTT Postgraduate Conference.

**Yuan Ping** received the B.S. degree in mechanical and electrical engineering and the M.S. degree in electrical engineering from Xidian University, Xi'an, China, in 2016 and 2019, respectively. She is currently working toward the Ph.D. degree in electrical and electronic engineering with the University of Hong Kong, Hong Kong.

Her research interests include EMI/PI/SI, computational electromagnetics, and data-driven and uncertainty quantification.

**Lijun Jiang** (Fellow, IEEE) received the B.S. degree from the Beijing University of Aeronautics and Astronautics, Beijing, China, in 1993, the M.S. degree from Tsinghua University, Beijing, China, in 1996, and the Ph.D. degree from the University of Illinois at Urbana-Champaign, Champaign, IL, USA, in 2004, all in electrical engineering.

From 1996 to 1999, he was an Application Engineer with the Hewlett-Packard Company. In 2004, he was the Postdoctoral Researcher, the Research Staff Member, and the Senior Engineer with IBM T. J. Watson Research Center, Yorktown Heights, NY, USA. In 2009, he was an Associate Professor with the Department of Electrical and Electronic Engineering, University of Hong Kong (HKU), where he received his Tenure in 2014. Since September 2014, he has been a frequent Visiting Scholar with the University of California at Los Angeles, Los Angeles, CA, USA. His research interests include large-scale heterogeneous electromagnetics, computational electromagnetics for VLSI signal and power integrity, EMC/EMI, nanoscale electromagnetism for THz and optoelectronics, antenna technologies, and microwave engineering for Internet of Things (IoT).

Dr. Jiang is an ACES Fellow, the Associate Editor of IEEE TRANSACTIONS ON ANTENNAS AND PROPAGATION, the Associate Editor of *Progress in Electromagnetics Research*, the Associate Editor of *ACES Express*, the Associate Guest Editor of the Proceedings of IEEE Special Issue in 2011–2012, etc. He has been the TPC Chair and the General Co-Chair of many international conferences and workshops. He has been active in most first-tier electromagnetics-related international symposiums and forums. His research team at HKU has received numerous international awards and honors, including IEEE EMC Technical Achievement Award, Best Conference Paper Awards, Best Student Paper Awards, Young Scientist Awards, etc.

**Hong Tat Ewe** (Senior Member, IEEE) received the B.Eng. degree (Hons.) in electrical engineering from the University of Malaya, Kuala Lumpur, Malaysia, in 1992, the M.Sc. degree in electrical engineering and computer science from the Massachusetts Institute of Technology, Cambridge, MA, USA, in 1994, and the Ph.D. degree in electrical engineering from Multimedia University, Cyberjaya, Malaysia, 1999.

He is currently a Senior Professor with the Lee Kong Chian Faculty of Engineering and Science, Kajang, Malaysia and the President of the Universiti Tunku Abdul Rahman, Kampar, Malaysia. He has authored or coauthored books, international journals and conferences, and newspaper column articles. His research interests include microwave remote sensing, satellite image processing, wireless sensor network, and intelligent computing.

Dr. Ewe is a Fellow of the ASEAN Academy of Engineering and Technology and the Academy of Sciences Malaysia.